



Universiteit
Leiden
The Netherlands

Complex processes in simple ices : laboratory and observational studies of gas-grain interactions during star formation

Öberg, K.I.

Citation

Öberg, K. I. (2009, September 16). *Complex processes in simple ices : laboratory and observational studies of gas-grain interactions during star formation*. Retrieved from <https://hdl.handle.net/1887/13995>

Version: Not Applicable (or Unknown)
License: [Leiden University Non-exclusive license](#)
Downloaded from: <https://hdl.handle.net/1887/13995>

Note: To cite this publication please use the final published version (if applicable).

2 THE *c2d* SPITZER LEGACY: ICE FORMATION IN STAR-FORMING REGIONS

The *Spitzer Space Telescope* observed ices towards an unprecedented number of protostars during its five-year mission. Within the *c2d* legacy program more than 40 low-mass protostars have been analyzed for ice features in a series of papers including CH₄ ice in Chapter 3. The *c2d* data are here combined with ice observations from other *Spitzer* programs, and previous VLT and *ISO* data, to construct a general ice formation scenario. The analysis reveals that low- and high-mass protostars mainly differ in their content of CO, CH₄ and CO₂ ice. Within the low-mass sample, the variability with respect to H₂O ice, described by the standard deviation of the log-transformed abundances, of 19 unique ice components ranges from 0.1 to 1.1. Combining the analysis of abundance variations, ice maps and ice correlations, shows that ices form sequentially and that large abundance variations are mainly due to formation pathways depending on different prestellar CO freeze-out rates and protostellar heating. The first step in the ice formation sequence is hydrogenation of atoms, resulting in e.g. H₂O, CO₂:H₂O, CH₄, NH₃. From their almost constant abundances, this stage must be similar for all low-mass star formation. A second formation wave is due to reactions with accreted CO ice and possibly energetic processing of H₂O-rich ices in the cloud core, resulting in CO₂:CO, CO:H₂O, OCN⁻ and CH₃OH ice. These formation yields depend on the collapse time scale and prestellar densities, and as a result the ice abundances vary by an order of magnitude between different protostars. Third, some ice components, e.g. pure CO₂ and CH₃CH₂OH, form at higher temperatures following the turn-on of the protostar because of diffusion and desorption of ices. CH₃CH₂OH ice is an excellent fit for the 7.25 μm feature and may thus be possible to detect towards a range of objects.

Öberg et al., in preparation

2.1 Introduction

Grain surface chemistry is the proposed source of the simplest hydrogenated molecules, H_2 , H_2O and CH_4 , as well as the complex organics molecules detected in the gas phase around protostars (Tielens & Hagen 1982; Garrod et al. 2008). It is now more than three decades since the first ices were detected in the interstellar medium, but it was only with the advent of the *Spitzer Space Telescope* that ice abundances could be investigated towards a large number of lines of sight at reasonable integration times.

During the last five years *Spitzer* observed ices towards more than 40 low-mass protostars within the *c2d* program (Boogert et al. 2008; Pontoppidan et al. 2008; Öberg et al. 2008, Bottinelli et al. in prep, from now on Paper I-IV) and dozens of more within other programs (e.g. Zasowski et al. 2009), providing an unprecedented sample-size of protostellar ice sources. In addition, *Spitzer* has detected ices towards several background sources, looking through molecular clouds at a range of extinctions (e.g. Bergin et al. 2005; Knez et al. 2005), although the densest parts of prestellar cores are still inaccessible. Neither kind of observations were possible over the full 5–30 μm infrared spectral region towards low-mass protostellar sources before *Spitzer* and its sensitive detectors. The spectral cut-off of *Spitzer* at 5 μm entails, however, that the spectra must be complimented with ground-based observations to cover the strongest H_2O transition at 3 μm , the only CO transition at 4.65 μm , and the XCN feature at 4.5 μm , and thus to achieve a comprehensive picture of ice abundances during star formation (Pontoppidan et al. 2003; van Broekhuizen et al. 2005). Building on these previous studies and introducing new ice data, this study aims to provide a general scenario of ice evolution during low-mass formation by combining statistics on ice abundances with protostellar ice maps, spectral analysis and comparison with previous high-mass data.

Such a general scenario has been presented for ice formation during high-mass star formation from analysis of spectra from the *Infrared Space Observatory (ISO)* of both protostars and background sources (Gibb et al. 2000, 2004). From comparison between protostars and background stars, H_2O and CO_2 were found to have a quiescent cloud origin. Many other ices, e.g. CH_4 , NH_3 and CH_3OH , were only detected towards protostars, but because of high upper limits Gibb et al. (2004) did not use this to exclude a cloud formation route for CH_4 and NH_3 , especially since the CH_4 abundances are almost constant within the protostellar sample. CH_3OH abundances are in contrast highly variable between different high-mass protostars, which was explained by formation from intense UV or thermal processing. The XCN feature, as well, varied by an order of magnitude within the sample and a similar protostellar origin was thus inferred. In summary the ice formation, processing and destruction were proposed to proceed in four steps (Gibb et al. 2000, 2004).

1. H_2O , CO_2 and probably CH_4 and NH_3 ices form together in a H_2O -rich ice component during the prestellar stage by surface reactions.
2. CO and probably O_2 and N_2 ices form by direct freeze-out in a separate ice component, which is also present before the turn-on of the protostar.

3. Mild energetic processing, always present around high-mass protostars, results in CO₂ formation in the CO-rich ice and some evaporation of CO ice. It also cannot be excluded that CH₄ and NH₃ form at this stage since they are not observed in the pre-stellar stages. Simultaneously a third ice component consisting of CH₃OH and CO₂ forms.
4. Finally, after intense UV and thermal ice processing towards a few high-mass protostars, large amounts of CH₃OH and XCN form in the H₂O-rich ice and all pure CO ice evaporates.

Two of the above conclusions come from analysis of the CO₂ spectra. First, a CO₂ spectral wing observed towards the protostars is produced in the laboratory when CH₃OH mixed with CO₂ ice. Second, pure CO₂ ice can be produced by ice segregation and this was used to explain the presence of pure CO₂ ice spectra in the *ISO* sample (Ehrenfreund et al. 1998). More generally, laboratory spectroscopy has demonstrated that the spectral profiles of all astrophysically relevant ices depend on whether the ice is pure or in an ice mixture and also on the composition of the ice mixture (e.g. Hagen et al. 1980; Sandford & Allamandola 1990, Chapter 4). As seen with the CO₂ profile, this is used when interpreting astrophysical spectra to determine the structure of interstellar ices in addition to the abundances of the detected species. While the exact ice environment is difficult to ascertain, the profiles of pure ices, of ices in a hydrogen-bonded ice, e.g. H₂O-dominated, and in a CO-rich ice can usually be distinguished. In the analysis of ground-based, and *Spitzer* observations alike this is used to determine the amount of the most common molecules that reside in a H₂O-rich ice, in a CO-rich ice and in a pure phase. This is important since observations suggest that most astrophysical ices consist of H₂O-rich layer, covered by a CO-rich layer (Pontoppidan et al. 2008).

Parts of the *ISO* ice formation scheme has been challenged by ground-based observations of abundant CH₃OH ice towards low-mass protostars (Pontoppidan et al. 2003), demonstrating that no intense processing is required for its formation – most ice around low-mass protostars is protected from stellar UV-light. The XCN feature was also observed to be common in a large sample of low-mass protostars, though its band position appears shifted to higher frequencies compared to the high-mass sources (van Broekhuizen et al. 2005). Van Broekhuizen et al. (2005) decomposed the observed band into two different components, one of which compares well with laboratory studies of OCN⁻. The origin of the second component is contested and suggested carriers include chemisorbed CO on silicate grains (Fraser et al. 2005) in addition to different CN-containing molecules. In general the XCN carrier towards high-mass protostars is dominated by the OCN⁻ component, while low-mass protostars contain both components at a variable ratio. The band may thus have two different carriers, one which depends on stellar processing, and one which does not.

During the same period Pontoppidan et al. (2003) developed a new framework for analyzing the ice structure and evolution while investigating the CO-ice feature towards a sample of 39 low-mass protostars, many of them the same as studied with *Spitzer*. Rather than directly comparing each observation with laboratory spectra, Pontoppidan

et al. (2003) decomposed, phenomenologically, all observed CO ice spectral profiles into three unique components. These three components were then compared with laboratory spectra and could be assigned to pure CO ice, CO mixed with H₂O or CH₃OH ice, and a component identified with some CO in a CO₂-rich ice mixture (confirmed in Paper II). This approach requires a large data sample, but it also offers several advantages in comparison with the traditional source-by-source comparison with spectra of different laboratory ice mixtures (e.g. Merrill et al. 1976; Gibb et al. 2004; Zasowski et al. 2009). First it avoids the ‘mix-and-match’ problem; often a range of different ice mixtures are consistent with the shape of a spectral feature because several ice-mixture components affect the spectral profiles of e.g. CO and CO₂ similarly. A mix and match of laboratory spectra to produce the observed features thus says little about the range of possible ice compositions consistent with the spectral profiles. Second, the phenomenological decomposition ensures a consistent treatment of all kinds of sources, since the scaling of different components can be done automatically to the spectral profile without subjective preconceptions on what the ice mixture should contain towards certain objects. Third, the phenomenological division of a common spectral feature into a minimum number of components provides information on the sample as a whole, i.e. it directly shows which parts of the spectral profile are ubiquitous and which are environment dependent. This is crucial information when assigning a component carrier – without this, the degeneracy is almost always too large to say much at all about the structure of the ice from a spectral profile analysis. So far the component analysis approach has been applied to the CO ice band, the XCN-band, the CO₂ ice feature and the 5–7 μ m complex within the *c2d* program and an overlapping ground-based observational program (Pontoppidan et al. 2003; van Broekhuizen et al. 2005, Paper I,II).

A second advance in the studies of ice formation is the construction of ice maps from samples of low-mass protostars in the same cloud core. Pontoppidan et al. (2004) constructed such a map of CH₃OH and H₂O ice abundances towards the SMM4 protostellar envelope in Serpens, demonstrating that the CH₃OH formation is a local process. In a map of the Ophiuchus F core Pontoppidan (2006) showed that the abundances of CO₂, of CO mixed with H₂O and of CO ice generally all increase towards the cloud core, but the CO increase is most dramatic of the three, tracing the ‘catastrophic’ freeze-out of CO at high densities.

The key conclusions on ices during low-mass star formation coming out from the statistical studies and the ice maps so far are that a H₂O-rich ice forms first in the prestellar phase, containing trace amounts of CH₄ and NH₃, and large amounts of CO₂ mixed into it. Later in the cloud-core phase, pure CO ice freezes out on top of this ice mixtures and a second CO₂ formation phase takes place resulting in a CO dominated CO:CO₂ ice mixture. Once the protostar turns on, the CO ice is distilled from the ice mixture, resulting in a pure CO₂ ice. Close to the protostar, the water-rich ice will also start to segregate resulting in more pure ice layers. The origins of CH₃OH ice, the XCN band and the proposed NH₄⁺ ice – the species thought to be responsible for the bulk of the 6.85 μ m band – remain unclear. NH₄⁺ is one of several tentative band assignments, including HCOOH and HCOO⁻, in Paper I that requires further analysis. Most of the unassigned ice bands fall within 5–8 μ m because of the complex absorption pattern of most organic

and nitrogen-bearing species in this spectral region. One the goals of this chapter is to further constrain their carriers.

The overall aim of this chapter is to identify under which conditions the carriers of observed ice features form. This is pursued by combining the observational results from the four *c2d* ice survey papers with previous VLT surveys of CO and XCN⁻ ice data, nine additional low-mass ice sources observed with *Spitzer* outside of the *c2d* program and the *ISO* results on high-mass sources to analyze global trends and variations in ice abundances towards low-mass and high-mass protostars, with focus on the larger low-mass sample. Section 2.2 summarizes the observations and the analysis procedure applied to old as well as new observational data. Section 2.3 first identifies the most variable ice features using histograms and calculated standard deviations. The reasons for abundance variations is then explored through protostellar ice maps, abundance correlation plots and a principal component analysis of the low-mass sample. The results are discussed in §2.4 with respect to different ice formation scenarios, ice chemistry in low-mass versus high-mass star-forming regions and the identification of ice features in crowded spectral regions, including some new spectral comparisons. The results of this chapter will be incorporated in a future paper, which will contain additional ice data on background stars and low-mass protostars in isolated cores.

2.2 Observations and spectral analysis

Spitzer-IRS spectra were obtained as part of the *c2d* Legacy program (PIDs 172 and 179) as well as a dedicated open time program (PID 20604) and a few archival spectra observed as part of the GTO programs of Houck et al. Most sources in the sample were included in Papers II-III and thus have reported CO₂ and CH₄ ice abundances, while the *c2d* sources alone were investigated in Paper I and IV. The entire sample is listed in Table 2.1.

Of the sources not included in Papers I and IV, we have derived the NH₃ and CH₃OH ice abundances or upper limits and the 5–7 μm components strengths following the procedures previously described in Papers I and IV. In summary, five different components C1–5 are fitted to the 5–7 μm complex and their relative optical depths are reported in Table 2.2. The NH₃ and CH₃OH abundances towards the same sources are determined from their 9.0 and 9.7 μm features, using one of the methods in Paper IV, where the underlying silicate feature is removed by fitting a 4th order polynomial to the silicate band. Three possible sets of points are tested for defining the continuum and the variation in the resulting column densities are included when estimating the uncertainty in the derived abundances. After continuum subtraction, the NH₃ and CH₃OH integrated optical depths are derived by fitting two Gaussians to the observed spectra around the expected band positions, based on laboratory spectra, and integrating the Gaussian fits. The resulting abundances are reported in Table 2.3. Paper I also reported NH₄⁺ and HCOOH abundances, but because of their contested assignments no additional NH₄⁺ and HCOOH abundances are reported here. The NH₄⁺ abundances, as defined in Paper I, are however included indirectly since they were derived from the sum of the C3 and C4 abundances.

Table 2.1. The source sample of 56 low-mass YSOs and 2 background stars observed with *Spitzer*-IRS and 8 high-mass YSOs observed with *ISO*.

Source	Alias	RA J2000	Dec J2000	Cloud	Type
L1448 IRS1		03 25 09.4	+30 46 21.7	Perseus	low
L1448 NA		03 25 36.5	+30 45 21.4	Perseus	low
IRAS 03235+3004		03:26:37.5	+30:15:27.9	Perseus	low
IRAS 03245+3002		03:27:39.0	+30:12:59.3	Perseus	low
L1455 SMM1		03:27:43.3	+30:12:28.8	Perseus	low
RNO 15		03 27 47.7	+30 12 04.3	Perseus	low
IRAS 03254+3050		03:28:34.2	+31:00:51.2	Perseus	low
IRAS 03271+3013		03 30 15.2	+30 23 48.8	Perseus	low
B1-a		03 33 16.7	+31 07 55.1	Perseus	low
B1-c		03:33:17.9	+31:09:31.0	Perseus	low
B1-b		03:33:20.3	+31:07:21.4	Perseus	low
IRAS 03439+3233	B5 IRS3	03 47 05.4	+32 43 08.5	Perseus	low
IRAS 03445+3242	B5 IRS1	03 47 41.6	+32 51 43.8	Perseus	low
L1489 IRS	IRAS 04016+2610	04:04:43.1	+26:18:56.4	Taurus	low
IRAS 04108+2803		04:13:54.72	+28:11:32.9	Taurus	low
HH 300		04:26:56.30	+24:43:35.3	Taurus	low
DG Tau		04:27:02.66	+26:05:30.5	Taurus	low
IRAS 08242-5050	HH46 IRS	08:25:43.8	-51:00:35.6	HH46	low
IRAS 12553-7651		12:59:06.6	-77:07:40.0	Cha	low
IRAS 13546-3941		13:57:38.94	-39:56:00.2	BHR92	low
IRAS 15398-3359		15:43:02.3	-34:09:06.7	B228	low
GSS 30 IRS1		16:26:21.4	-24:23:04.1	Ophiuchus	low
WL 12		16:26:44.2	-24:34:48.4	Ophiuchus	low
Elias 29		16:27:09.42	-24:37:21.1	Ophiuchus	low
GY 224		16:27:11.2	-24:40:46.7	Ophiuchus	low
WL 20		16:27:15.7	-24:38:45.6	Ophiuchus	low
IRS 37		16:27:17.6	-24:28:56.5	Ophiuchus	low
WL 6		16 27:21.8	-24:29:53.3	Ophiuchus	low
IRS 42		16:27:21.5	-24:41:43.1	Ophiuchus	low
CRBR 2422.8-3423		16:27:24.61	-24:41:03.3	Ophiuchus	low
IRS 43		16:27:27.0	-24:40:52.0	Ophiuchus	low
IRS 44		16:27:28.1	-24:39:35.0	Ophiuchus	low
Elias 32	IRS 45	16:27:28.4	-24:27:21.4	Ophiuchus	low
IRS 46		16:27:29.4	-24:39:16.3	Ophiuchus	low
VSSG 17	IRS 47	16:27:30.2	-24:27:43.4	Ophiuchus	low
IRS 51		16:27:39.8	-24:43:15.1	Ophiuchus	low
IRS 63		16:31:35.7	-24:01:29.5	Ophiuchus	low
L1689 IRS5		16:31:52.1	-24:56:15.2	Ophiuchus	low
RNO 91	IRAS 16316-1540	16:34:29.3	-15:47:01.4	L43	low
IRAS 17081-2721		17:11:17.28	-27:25:08.2	B59	low
B59 YSO5		17:11:22.2	-27:26:02.3	B59	low
2MASSJ17112317-2724315		17:11:23.1	-27:24:32.6	B59	low
EC 74		18:29:55.72	+01:14:31.6	Serpens	low
EC 82		18:29:56.89	+01:14:46.5	Serpens	low
SVS 4-5	EC 88	18:29:57.6	+01:13:00.6	Serpens	low
EC 90		18:29:57.75	+01:14:05.9	Serpens	low
EC 92	SVS 4-10	18:29:57.9	+01:12:51.6	Serpens	low
CK4		18:29:58.21	+01:15:21.7	Serpens	low
CrA IRS 5		19:01:48.0	-36:57:21.6	Corona Australis	low
HH 100 IRS		19:01:50.56	-36:58:08.9	Corona Australis	low
CrA IRS7 A		19:01:55.32	-36:57:22.0	Corona Australis	low
CrA IRS 7 B		19:01:56.4	-36:57:28.0	Corona Australis	low
CrA IRAS32		19:02:58.7	-37:07:34.5	Corona Australis	low
L1014 IRS		21:24:07.5	+49:59:09.0	L1014	low
IRAS 23238+7401		23:25:46.65	+74:17:37.2	CB 244	low
W3 IRS5		02 25 40.8	+62 05 52.8		high

2.2 OBSERVATIONS AND SPECTRAL ANALYSIS

Table 2.1 (cont'd)

Source	Alias	RA J2000	Dec J2000	Cloud	Type
MonR2 IRS3		06:07:47.8	-06:22:55.0		high
GL989		06:41:10.1	+0.9:29:35.8		high
W33A		18:14:39.4	-17:52:01.3		high
GL 2136		18 22 27.0	-13 30 10.0		high
GL7009S		18:34:20.9	-05:59:42.2		high
S140 IRS1		22:19:18.17	+63:18:47.6		high
NGC7538 IRS9		23:14:01.6	+61:27:20.2		high
Elias 16		04:39:38.88	+26:11:26.6	Taurus	bg
EC 118	CK 2	18:30:00.62	+01:15:20.1	Serpens	bg

Table 2.2 – Optical depths of the 5–7 μm complex components for new sources.

Source	τ_{C1} (5.84 μm)	τ_{C2} (6.18 μm)	τ_{C3} (6.76 μm)	τ_{C4} (6.94 μm)	τ_{C5} (broad)
WL 12	0.012 \pm 0.003	0.000 \pm 0.002	0.049 \pm 0.004	0.136 \pm 0.003	0.014 \pm 0.071
WL 6	0.002 \pm 0.007	0.000 \pm 0.006	0.137 \pm 0.007	0.087 \pm 0.006	0.030 \pm 0.045
IRS 42	–	–	–	–	–
IRS 43	0.059 \pm 0.004	0.082 \pm 0.003	0.179 \pm 0.005	0.105 \pm 0.004	0.066 \pm 0.051
IRS 44	0.080 \pm 0.005	0.089 \pm 0.004	0.135 \pm 0.005	0.201 \pm 0.004	0.004 \pm 0.086
Elias 32	0.021 \pm 0.005	0.000 \pm 0.004	0.050 \pm 0.009	0.075 \pm 0.007	0.058 \pm 0.025
IRS 46	0.018 \pm 0.004	0.002 \pm 0.004	0.076 \pm 0.005	0.066 \pm 0.004	0.000 \pm 0.023
VSSG17	0.058 \pm 0.002	0.056 \pm 0.002	0.042 \pm 0.005	0.061 \pm 0.004	0.011 \pm 0.016
IRS 51	0.042 \pm 0.003	0.036 \pm 0.002	0.074 \pm 0.003	0.060 \pm 0.002	0.000 \pm 0.012
IRS 63	0.000 \pm 0.003	0.023 \pm 0.002	0.048 \pm 0.003	0.060 \pm 0.003	0.044 \pm 0.039

Table 2.3 – Ice column densities and abundances for new sources.

Source	N(H ₂ O) 10 ¹⁷ cm ⁻²	[NH ₃] %	[CH ₃ OH] %
WL 12	22.1 \pm 3.0	<3.8	<4.5
WL 6	41.7 \pm 6.0	2.9 \pm 0.4	<2.1
IRS 42	19.5 \pm 2.0	<2.1	11.9 \pm 1.1
IRS 43	31.5 \pm 4.0	–	–
IRS 44	34.0 \pm 4.0	3.7 \pm 0.4	<1.6
Elias 32	17.9 \pm 2.6	<5.2	12.4 \pm 1.9
IRS 46	12.8 \pm 2.0	5.1 \pm 0.9	<4.1
VSSG 17	17.0 \pm 2.5	<3.1	6.9 \pm 2.4
IRS 51	22.1 \pm 3.0	2.4 \pm 0.3	11.7 \pm 0.9
IRS 63	20.4 \pm 3.0	5.7 \pm 1.3	<1.8

2.3 Results

The complete ice data set contains seven identified molecules – H₂O, CO₂, CO, CH₄, NH₃, CH₃OH and OCN⁻ – seven additional features attributed to CO and CO₂ (here and in the remainder of the chapter X:Y denotes species X found in an X:Y ice mixture) in different ice environments and seven ice components, yet to be firmly identified with a single carrier. The XCN feature decomposition in van Broekhuizen et al. (2005) is adopted consisting of features at 2165 (OCN⁻) and 2175 cm⁻¹. The band assigned to HCOOH at 7.25 μm is included as the ‘7.25 μm band’. The range of ice abundances with respect to H₂O ice is presented in histogram form and parameterized with the standard deviation of the log-transformed abundances with respect to H₂O ice in §2.3.1. The sources of abundance variations for different species are then explored through correlation plots, ice mapping of the Oph-F core and a principal component analysis of the ice abundances.

2.3.1 Abundance variations of different ices

There are ice components with small deviations and others with a much broader observed range between different sources. This is illustrated in Fig. 2.1, which shows a direct comparison between a narrow (CO₂) and a broad (CH₃OH) ice abundance distribution. The CH₃OH ice abundance uncertainties are 5–30% (0.02–0.13 when log-transformed) and the CO₂ uncertainties are only a few percent. The difference in abundance variation is thus real. For most ice components presented in Fig. 2.2–2.4, the relative abundance uncertainty is less than 10%. Exceptions are CH₄, NH₃, OCN⁻, XCN, the 2175 cm⁻¹ feature, the 7.25 μm band and CH₃OH, which have uncertainties up to 30%. As reported below, all ices have log-transformed standard deviations above 0.1, equivalent to 30%, and thus ice abundance uncertainties do not alone explain the differences in ice abundance variations.

Figures 2.2–2.4 show the spread in ice abundances for all detected ice features, including significant upper limits, where the ice abundances with respect to the median have been log-transformed (power 10). The OCN⁻ abundances in Fig. 2.2 are derived from the 2165 cm⁻¹ component in agreement with laboratory OCN⁻ spectra, while ‘2175 cm⁻¹’ is the optical depth of the second XCN component and ‘XCN’ encompasses the entire feature.

Each histogram is centered on the median ice abundance with respect to H₂O ice, where the median is calculated from the detected ice abundances towards the low-mass protostars. The histogram bins are calculated from the variance among the detected ice abundances towards the same sample. Most histograms include only ice detections. The plots for OCN⁻, XCN, the 2175 cm⁻¹ feature, CH₃OH and NH₃ include upper limits as well, since most upper limits for these species lie below the median detected abundance and are thus significant. The high-mass protostellar abundance histograms are overplotted based on the median and bin size derived from the low-mass protostellar abundances. Table 2.4 lists the standard deviation from the median of the log-transformed abundances for all low-mass protostellar ices, in increasing order, which can be used as a numerical measure of the ice abundance variability during this star-formation stage. Table 2.4

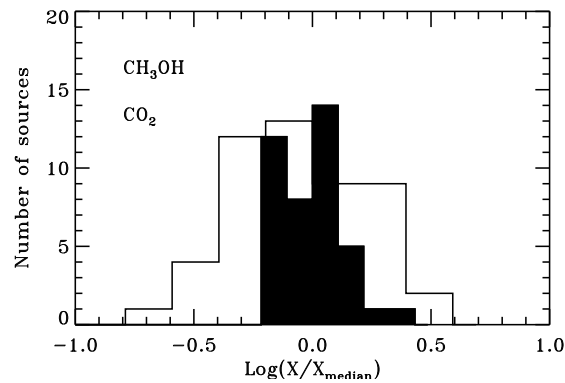


Figure 2.1 – Histograms of the CO_2 (solid) and CH_3OH ice abundances (black contours) towards low-mass protostars, illustrating the difference between an ice component with a narrow (CO_2) and a broad (CH_3OH) abundance distribution. The ice abundances are with respect to H_2O ice and are normalized to the median of each ice abundance.

also include commonly proposed formation mechanisms and identifications from previous studies; UV or ion processing can produce most molecules but is only listed specifically where there are observations that suggest this formation pathway.

CO_2 , CH_4 and NH_3 have all been suggested to form in the quiescent clouds. This is consistent with their narrow distributions and log-transformed standard deviations of <0.2 ; this early formation should be the least sensitive to cloud collapse time scales and thus to the evolutionary stage of the material in front of the protostar, which may either be dominated by the protostellar envelope or the surrounding cloud.

Among the total ice abundances, CO , OCN^- and CH_3OH have the broadest distributions for the low-mass protostars, i.e. there are order of magnitude abundance variations between different sources, and the log-transformed standard deviations are >0.2 . OCN^- and CH_3OH cover a similar abundance range towards the smaller high-mass sample, while the CO abundances towards the high-mass protostars are consistently low. The high-mass protostellar total ice abundances are also separated from their low-mass counterparts for CO_2 and CH_4 , where the high-mass abundances peak at a significantly lower level. Among the XCN components, the high-mass sample is slightly shifted to higher abundances for OCN^- and the total XCN components, and to lower abundances for the 2175 cm^{-1} component.

The CO and CO_2 component histograms are shown in Fig. 2.3. The $\text{CO}_2:\text{H}_2\text{O}$ component distribution towards low-mass protostars is narrow, while all other abundances have log-transformed standard deviations of >0.2 . The pure CO and CO_2 ice components are very broad in the low-mass sample, consistent with their predicted dependence on the envelope temperature. The component plots also reveal that the difference in CO_2 abundances between low-mass and high-mass stars is due to a difference in $\text{CO}_2:\text{H}_2\text{O}$; the other component abundances are not significantly different between the low-mass and

Table 2.4 – Standard deviations (SD) of log-transformed ice abundances, including upper limits (UL), and proposed carriers and surface formation pathways.

Ice feature	SD	SD UL	Proposed carriers	Formation pathways
C3	0.10		$\text{NH}_4^+ + \text{CH}_3\text{OH}^1$	NH_4^+ : acid-base chemistry ^{2,3,4}
CO_2	0.11			$\text{CO} + \text{O}(\text{H})^5$
$\text{CO}_2:\text{H}_2\text{O}$	0.12			$\text{CO} + \text{OH}^6$
7.25 μm	0.14		(HCOOH^1)	$\text{HCO} + \text{OH}^5$
NH_3	0.15	0.16		hydrogenation of N^5
CH_4	0.17			hydrogenation of C^5
C4	0.17		$\text{NH}_4^+{}^1$	heated NH_4^+ ice ¹
$\text{CO}_2:\text{CO}$	0.21			$\text{CO} + \text{O}(\text{H})$, UV/ion + $\text{CO}^{5,7,8}$
$\text{CO}:\text{H}_2\text{O}$	0.22			CO freeze-out and migration ⁷ , UV + H_2O + carbon grain ⁹ , UV + $\text{H}_2\text{O}:\text{CO}_2$ ice ¹⁰
CH_3OH	0.20	0.23		Hydrogenation of $\text{CO}^{11,12}$
C1	0.24		$\text{HCOOH} + \text{H}_2\text{CO}^1$	H_2CO : see CH_3OH
$\text{CO}:\text{CO}_2$	0.26			see $\text{CO}_2:\text{CO}$
XCN	0.21	0.27	$\text{OCN}^- + \text{CO}-\text{Si}^2$	see OCN^- and 3175 cm^{-1}
CO_2 shoulder 2175 cm^{-1}	0.28 0.17	0.29	$\text{CO}_2:\text{CH}_3\text{OH}^{13}$ $\text{XCN} + \text{CO}-\text{Si}^2$	co-formation $\text{CO}-\text{Si}$: chemisorption on on silicate grains ¹⁴
OCN^-	0.13	0.31		acid-base chemistry from $\text{NH}_3 + \text{HNCO}^2$ UV/ions + $\text{NH}_3 + \text{COX}$ ice
C5	0.31		warm H_2O + anions + refractory organics ¹	ice heating or acid-base chemistry or UV processing ¹
CO	0.31			freeze-out from gas-phase
C2	0.33		$\text{HCOO}^- + \text{NH}_3^1$	HCOO^- : acid-base chemistry from $\text{NH}_3 + \text{HCOOH}^1$
pure CO	0.38			see CO
pure CO_2	0.53	1.09		thermal heating of $\text{CO}_2:\text{CO}$ or of $\text{H}_2\text{O}:\text{CO}_2^{15}$

¹Paper I, ²van Broekhuizen et al. (2004), ³Schutte & Khanna (2003), ⁴Raunier et al. (2004), ⁵Tielens & Hagen (1982), ⁶Chang et al. (2007), ⁷Ioppolo et al. (2009), ⁸Paper II, ⁹Mennella et al. (2004), ¹⁰Gerakines et al. (2000), ¹¹Watanabe et al. (2003), ¹²Fuchs et al. (in press), ¹³Dartois et al. (1999), ¹⁴Fraser et al. (2005), ¹⁵Chapter 5.

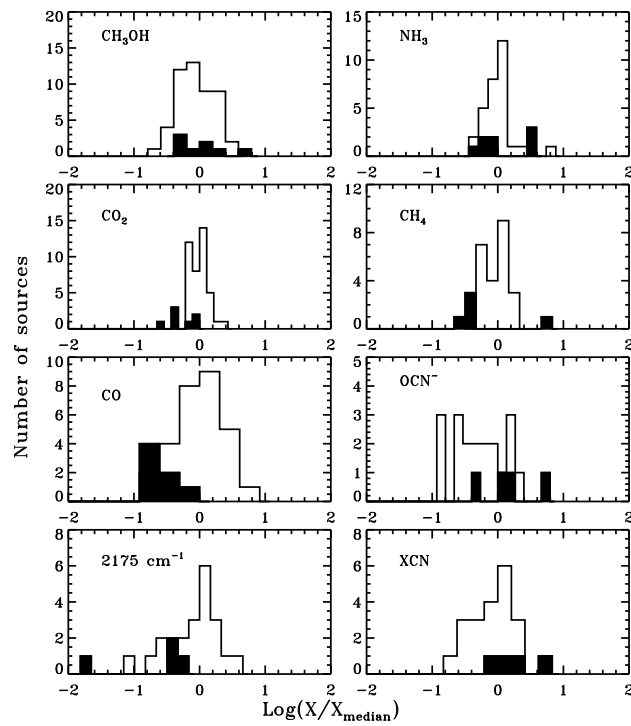


Figure 2.2 – Histograms of ice abundances towards low-mass protostars (black contours) and high-mass protostars (filled), where the ice abundances are with respect to H_2O ice and are normalized to the median of each ice abundance towards the low-mass protostars.

high-mass sample. All CO abundances are shifted to lower values for the high-mass sample, consistent with warmer envelopes around high-mass protostars compared to low-mass protostellar envelopes.

The $5\text{--}7 \mu\text{m}$ components, C1–5, and the $7.25 \mu\text{m}$ band span the full range of variations observed among the known ice abundances, from the extremely narrow distribution of C3 to the broad distributions of C2 and C5, while C1, C4 and the $7.25 \mu\text{m}$ bands are somewhere in between. This variation of the components with respect to H_2O ice was also noted in Paper I. The complexity and formation conditions of the carriers of these bands should thus cover the entire range of observed ice molecules. In Paper I, the $7.25 \mu\text{m}$ band is attributed to HCOOH , C1 to HCOOH and H_2CO , C2 to NH_3 and HCOO^- , C3 partly to CH_3OH and NH_4^+ , C4 to NH_4^+ and C5 has a number of potential carriers, including non-volatile organics and ions. The validity of especially the NH_4^+ , HCOOH and HCOO^- assignments is discussed further below.

To summarize, a large number of the investigated ices vary too much to form early on in the cloud together with H_2O and CO_2 . The following sections aim to constrain

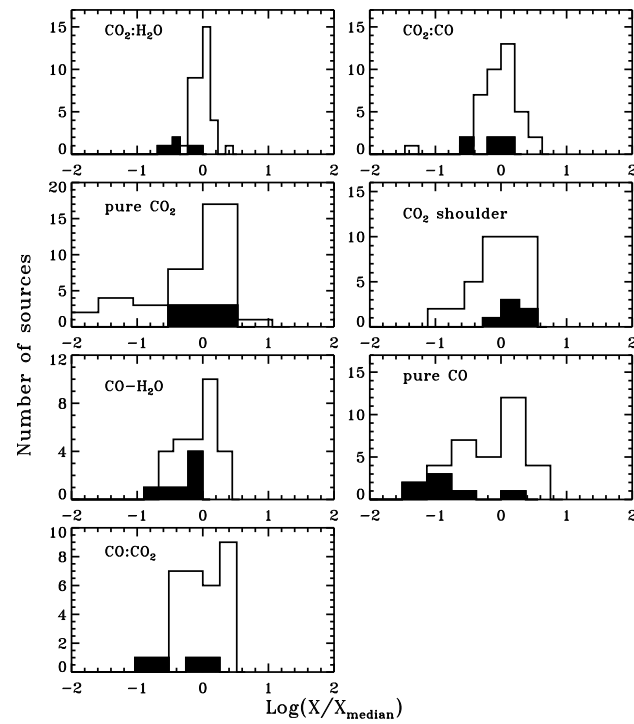


Figure 2.3 – Histograms of CO and CO₂ ice component abundances where X:Y should be read as amount of X in an X:Y mixture. Otherwise as in Fig. 2.3

the reasons behind these abundance variations which may a priori be caused by several different factors including:

1. different initial chemical conditions in different star-forming clouds,
2. different prestellar evolution timescales affecting both the CO freeze-out and the ice exposure to cosmic rays and cosmic-ray induced UV radiation,
3. whether the material in front of the protostar originates in the envelope or the surrounding cloud material and thus its evolutionary stage,
4. protostellar heating of the ice mantles causing ice diffusion and desorption, and
5. destruction or formation from stellar UV radiation.

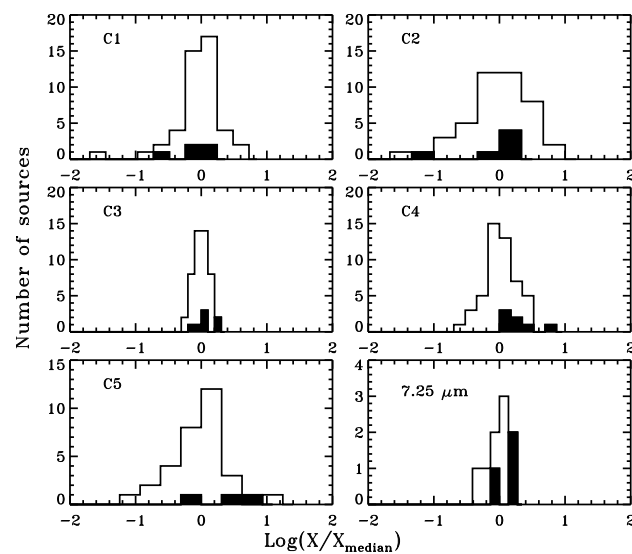


Figure 2.4 – Histograms of 5–7 μm component abundances and the 7.25 μm feature. Otherwise as in Fig. 2.2.

2.3.2 Protostars versus background stars

Only a handful of background stars have so far been investigated for ices within the *c2d* program, of which two were included in Paper I and one in Paper II. These two sources, Elias 16 and EC 118, are here used for comparison between quiescent clouds and protostars. H_2O , all CO_2 and CO components, except for pure CO_2 , and the C1-4 components are detected towards at least one of the background sources and thus do not require stellar processing to form. Of the undetected species, the upper limits for all features, except for pure CO_2 , are similar to the lowest abundances towards protostars. Hence, the current small sample of background sources do not provide any additional constraints on when and where these non-detected ices form.

2.3.3 Heating (in)dependencies

Protostellar ice heating was explored in Paper I and II as an underlying cause for observed abundance variations of the C1-5 components and CO_2 and CO ice. Ice heating is predicted to reduce the abundances of volatile ices, segregate previous ice mixtures and cause diffusion of ice radicals and thus the formation of more complex species. For example, pure CO ice evaporates already at low temperatures, while pure CO_2 is only expected to form after ice heating to at least 30 K from $\text{CO}_2:\text{CO}$ distillation or $\text{CO}_2:\text{H}_2\text{O}$ segregation (e.g. Chapter 5). The low abundances of CO and CH_4 ice towards high-mass stars confirm the sensitivity of volatile ices to the thermal envelope properties.

These well-understood dependencies of CO and CO₂ components on ice heating can be used to test the dependence of other ice components on ice heating. The two temperature tracers employed in Papers I and II are the fraction of CO in a H₂O-rich ice compared to pure CO ice and the fraction of CO₂ ice that is pure. The CO:H₂O component either form from chemistry inside the H₂O ice or through diffusion of CO into the H₂O ice upon heating. In either case CO:H₂O is less volatile than pure CO ice and the ratio should be temperature dependent.

Paper I found that the variation in C5 correlates with the fraction of CO in a H₂O-rich ice compared to pure CO ice, but only if high-mass sources are included. Excluding these high-mass sources removes the correlation. Furthermore, none of the other six most variable ice species (excluding CO and CO₂) are correlated with ice temperature tracers (either the CO or CO₂ ones) when only including the low-mass sample (not shown). Too many other factors may differ between low-mass and high-mass sources to deduce information about ice formation pathways including both types of objects in the same correlation plots, e.g. different formation pathways of similar features. Hence, except for the ice features already predicted to be temperature sensitive there is no additional evidence for the role of ice heating in simple ice formation. As discussed below it may still be needed to explain the presence of more complex ices indicated by the 7.25 μm feature, but there are too few detections of isolated complex ice features to check correlations.

2.3.4 Ice maps of the Oph-F core

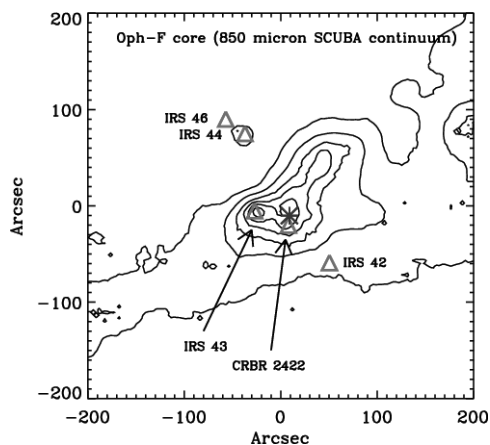


Figure 2.5 – A Scuba 850 μm map, tracing the dust emission of the Oph-F core taken from Pontoppidan (2006). The positions of the protostars in the ice map are marked with triangles.

A previous ice map of the Oph-F core revealed clear trends in the CO, CO₂ and CO:H₂O abundances; all three abundances decrease monotonically when the infrared sources are plotted versus distance away from the central core (Pontoppidan 2006). Note that the lines of sight to these sources probe primarily the dense quiescent core, rather

than ice formation during the protostellar phase. The same core is here mapped in all 19 ice features; Figure 2.5 shows the position of the protostars with respect to the Oph-F core. Figure 2.6 shows that most ice abundances have no clear trends with respect to the distance from the core. This is expected for species forming early during cloud formation (e.g. CH_4 and NH_3), which are independent of cloud core time scales and CO freeze-out, of species dependent on the protostar (e.g. pure CO_2 ice) and of components with multiple carriers as can be suspected for the C1-5 bands.

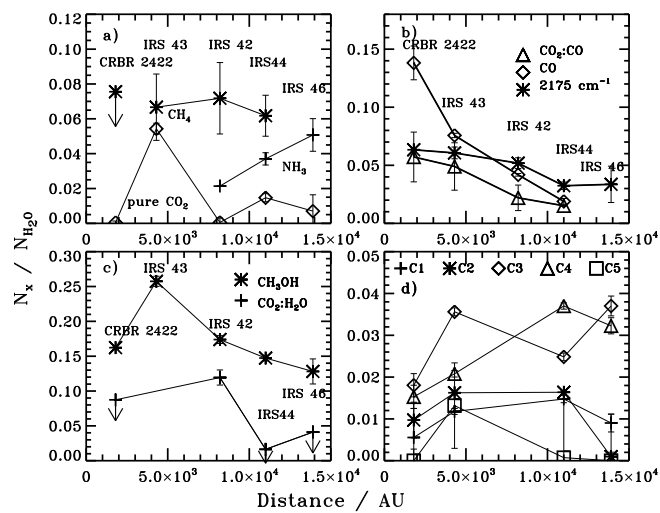


Figure 2.6 – Ice abundances at different distances towards the Oph-F core region. The 2175 cm^{-1} abundances are scaled by 20 and the CO abundances with 0.2 for clarity. The C1-C5 components are plotted optical depths scaled to the $3\text{ }\mu\text{m}$ H_2O ice feature since the band strengths of their carriers are unknown.

Of the three ices identified to increase towards the core by Pontoppidan (2006), the rapid and monotonic increase of the CO ice abundance towards the core region was interpreted as a catastrophic freeze-out of CO in the pre-stellar stage once a certain density and temperature is reached. The order of magnitude increase in CO ice with respect to H_2O is accompanied by a small increase the abundance of $\text{CO}:\text{H}_2\text{O}$ ice and a factor of three increase in the total CO_2 abundance, suggesting a CO_2 formation pathway from CO ice. This is confirmed in Fig. 2.6b, which shows that the $\text{CO}_2:\text{CO}$ increases towards the core. The only other species that increases monotonically towards Oph-F is the 2175 cm^{-1} band. OCN^- is not detected towards these sources and the 2175 cm^{-1} component is thus the entire XCN feature.

At least one other ice component, $\text{CO}_2:\text{H}_2\text{O}$, increases initially towards the core followed by a drop towards the centre-most source CRBR 2422.8-3423 (Fig. 2.6c). The pattern of CH_3OH and the C5 component is consistent with such a trend as well, but they are based on one detection and several upper limits each. This is consistent with that

$\text{CO}_2\text{:H}_2\text{O}$ and CH_3OH both have probable formation mechanisms that depend on the simultaneous presence of CO freeze-out and accreting H atoms and the gas phase H fraction should decrease towards the core. Thus the peak $\text{CO}_2\text{:H}_2\text{O}$ and CH_3OH abundances at a some distance from the core may be caused by prestellar conditions favouring CO and O hydrogenation outside of IRS 43, while all O or OH react with CO before a second H accretes onto the grain surface inside of IRS 43. $\text{CO}_2\text{:CO}$ may also form through cosmic rays and $\text{CO}+\text{O}$ reactions towards the center of the core.

No other ice abundances follow any trends towards the core, including the $7.25\ \mu\text{m}$ feature, the CO_2 shoulder and pure CO_2 ice, consistent with a map dominated by material in the quiescent cloud core.

2.3.5 XCN ice abundance correlations

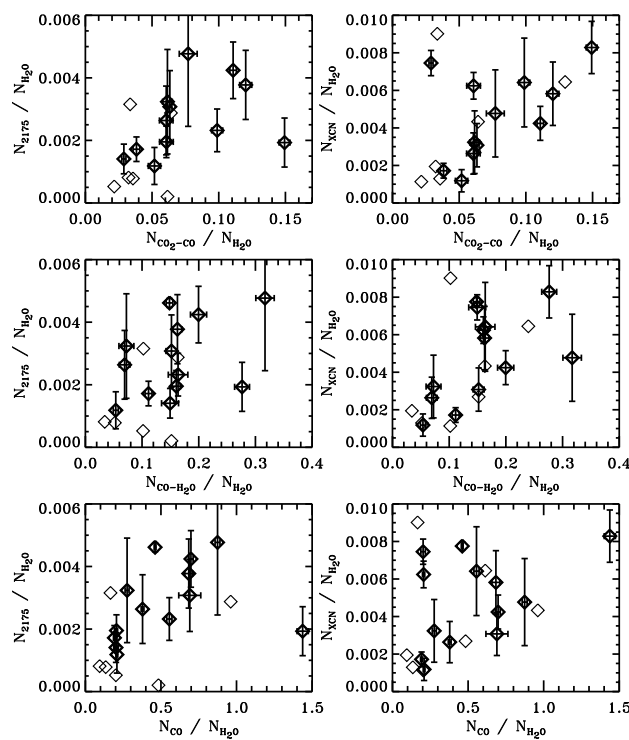


Figure 2.7 – Correlation plots of the total XCN band and the $2175\ \text{cm}^{-1}$ XCN component with $\text{CO}_2\text{:CO}$, $\text{CO:H}_2\text{O}$ and the total CO abundance, all with respect to H_2O ice. The grey diamonds are XCN and $2175\ \text{cm}^{-1}$ upper limits.

To test the XCN-related findings for the Oph-F core, correlations of CO-related species with the XCN components are investigated for the entire low-mass ice sample. Figure

2.7 shows that there is at best a tentative correlation between the 2175 cm^{-1} feature and $\text{CO}_2:\text{CO}$ and $\text{CO}:\text{H}_2\text{O}$ in the entire low-mass sample ($R=0.38$ and $R=0.41$). The correlations are stronger ($R=0.50$ and $R=0.56$, 12 mutual detections) and statistically significant at 95% level between the entire XCN feature and the same CO_2 and CO components. The correlations with the total CO abundance is weaker for both the 2175 cm^{-1} component and the entire XCN band, possibly because of the high volatility of CO compared to XCN. There are too few OCN^- detections towards low-mass protostars to carry out a similar correlation analysis. Thus, in a well constrained environment, i.e. the Oph-F core, the 2175 cm^{-1} component trace CO_2 present in a CO-rich ice and CO present in a H_2O -rich ice well, while in the sample as a whole the XCN band is better correlated with both. Both $\text{CO}:\text{H}_2\text{O}$ and $\text{CO}_2:\text{CO}$ are present towards quiescent lines of sight in clouds (Pontoppidan et al. 2003, Paper II). The correlations are thus indicative of a quiescently formed, CO-related, single carrier of the XCN band, with a varying profile dependent on the local environment.

2.3.6 Principal component analysis and ice abundance correlations

With 19 unique ice components, the number of possible correlations within the ice sample is large. Principal Component Analysis (PCA) offers a fast technique to reveal underlying structures in a multivariate sample by reducing the dimensions of the data set. This is done by projecting down both the sources and the source attributes, here the ice abundances with respect to H_2O ice, on principal components (PCs), which trace latent variables that govern the behavior of measurable quantities. In this data set, potential latent variables are the UV-field strength and the CO freeze-out fraction, which may govern the abundances of several of the observed spectral peaks.

The ice abundance data are projected onto principal components using the IDL routine *pca.pro*, which normalizes all data to zero mean and unity variance before calculating the eighteen eigenvectors of the data matrix, i.e. the principal components. The original ice abundance vectors are described perfectly by a combination of all principal components. The strength of PCA is that the principal components are chosen sequentially to explain the maximum variance in the data set. Therefore three principal components explain $\sim 50\%$ of the variation in this sample.

Figure 2.8 shows the sources and the ice abundances plotted with respect to the first three principal components. The sources have been color-coded based on their host cloud (see on-line version) and there are no apparent differences between the different cloud sources with respect to ice abundances. Initial cloud conditions are not then a source of ice abundance variations. IRS 51, EC 82 and EC 92 stand out in the source plots, demonstrating the potential use of PCA to detect special sources within large samples.

In the PCA ice abundances plots, species that appear close together are similarly described by the principal components in the plot and are thus likely correlated, especially if the same group re-occurs in different PC plots. Vice versa, species on opposite sides in the plot are anti-correlated. The first PC plot includes several expected groups such as CO and pure CO; $\text{CO}:\text{CO}_2$, $\text{CO}_2:\text{CO}$ and $\text{CO}:\text{H}_2\text{O}$; CO_2 , $\text{CO}_2:\text{H}_2\text{O}$ and the CO_2 shoulder. It also suggests that C1, C3 and NH_3 are related. When checked individually, the CO and

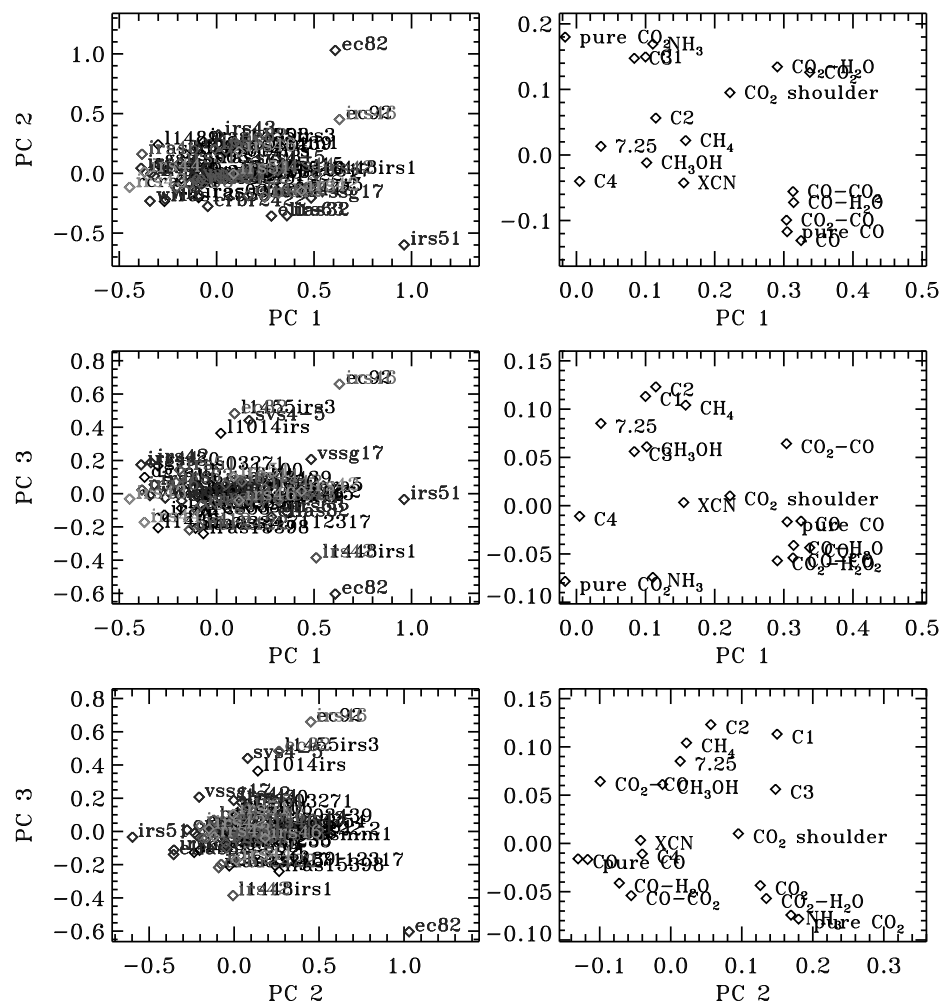


Figure 2.8 – Principal component analysis plots containing all low-mass sources and molecular detections. (In the online version the sources are color-coded with respect to star forming cloud: Ophiuchus = blue, Serpens = green, Perseus = red and CrA = orange.)

CO₂ species are all correlated significantly within each group at a 95-99.5% level. The proposed NH₃ correlations depend on a single source, EC 82, however and if this source is removed the NH₃ is no longer grouped with C1 and C3 in the PCA plot. C1 and C3 are correlated, though there is a large amount of scatter. In the PC1 versus PC3 plot, the C2 and C1 correlations with the 7.25 μm feature, and with CH₄ are significant, while there are too few overlaps between CH₄ and the 7.25 μm detections to evaluate their relationship. The other new groupings in the PC1 versus PC3 and PC2 versus PC3 are not significant, except for the XCN correlations already considered and C3 and the CO₂ shoulder.

PCA can thus not be used blindly to call species correlated, nor are all correlations visible when investigating only the first three PCs. The plots do, however, suggest several correlations that may otherwise not be investigated. The most significant discoveries in light of the further discussion are first that CO₂:CO is better correlated with the different CO abundances than with other CO₂ components, indicative of a universal conversion of pure CO ice into CO₂:CO during CO freeze-out. Second, the C3 correlations with C1 and the lack of correlation with NH₃ are important because of the suggested multiple carriers of C3, including H₂CO and NH₄⁺. Finally the relationship between C1, C2 and the 7.25 μm may provide evidence for complex ice formation as outlined further below.

The latent variables traced by PC1-3 are not obvious, but PC1 seems to generally trace the total CO and CO₂ ice abundances or CO freeze-out, PC2 depends on the CO versus CO₂ content or ice temperature and PC3 on the CH₄, C1, C2 and 7.25 μm feature abundances. This also explains some of the outlying sources – EC 82 is a warm source with silicate emission features, while IRS 51 contains an extremely large CO ice column, indicative of a low temperature environment. The latent variables thus suggest that CO freeze-out followed by new ice formation, ice heating, and potentially simple ice photolysis as traced by C1, C2 and 7.25 μm components, are the three most important factors for explaining ice abundance variations. This is consistent with the analysis in the previous sections, although the last PC assignment depends on what C1, C2 and the 7.25 μm features can be assigned to, which is the first topic of the next section.

2.4 Discussion

The previous section established that spectral ice features form during low-mass formation through a range of processes, some universally present, while others depend critically on the local pre- and proto-stellar conditions. Before discussing this further, the identifications of previously unassigned or tentatively assigned ice features are established following the constraints put on their carriers from the results and some new spectral comparisons §2.4.1. The sequential ice formation is then discussed followed by a preliminary comparison of low-mass versus high-mass ice sources and the proposed origin of their differences in ice abundances.

2.4.1 The XCN feature and other unidentified ice bands

The XCN feature can be at least partly assigned to OCN^- from comparison with laboratory spectra. The assignment of the 2175 cm^{-1} has been debated since laboratory OCN^- bands peak between 2155 and 2172 cm^{-1} (van Broekhuizen et al. 2004). The alternative assignment to CO-chemisorption onto silicate grains (Fraser et al. 2005) is however inconsistent with the increasing amount of the 2175 cm^{-1} carrier towards the Oph-F core region, where the grains should already be completely covered with the H_2O -rich ice. Proton bombardment of CO and N_2 containing ices does result in a new feature around 2180 cm^{-1} (Moore et al. 1983; Hudson et al. 2001), which may be the carrier of the 2175 cm^{-1} component towards protostars. The carrier is then most likely a radical, since it disappears at 35 K in the laboratory and this would explain its prevalence towards low-mass sources, and its low abundance towards high-mass ones. It is also consistent with the CO: CO_2 correlation, since it forms from CO in the laboratory.

As discussed above there is however evidence that the entire XCN feature is due to OCN^- ; 3 cm^{-1} is a relatively small frequency difference for an ice feature and OCN^- may not have been studied in an appropriate ice mixture yet. In a H_2O -rich ice mixture, the OCN^- band shifts to lower wave numbers at higher temperature, consistent with the trends of the XCN bands towards low-mass and high-mass sources. OCN^- formation should depend on CO freeze-out, since a plausible reaction pathway is radical chemistry of CO and NH to form HNCO, followed by proton-loss in the presence of a strong base. This assignment is thus also consistent with the observed correlations. OCN^- can also form through ion or UV bombardment of the H_2O -rich ice layer (van Broekhuizen et al. 2004), but this is harder to reconcile with the close relationship between the XCN feature and different CO-related features for the low-mass stars.

To conclusively settle between these different scenarios requires a number of studies. First an assignment to the reported 2180 cm^{-1} feature in the laboratory to investigate its plausibility as a carrier in space, second a more quantitative understanding of how HNCO and OCN^- form in interstellar ice analogues and third more cloud core observations to ensure that XCN generally forms towards cloud cores. Ice heating does however not seem necessary to form the XCN feature even though it may be responsible for its enhancement towards high-mass protostars. This is consistent with acid-base reactions, which are efficient already at 15 K (van Broekhuizen et al. 2005).

The $7.25\text{ }\mu\text{m}$ ice band has previously been assigned to HCOOH (Gibb et al. 2000, Paper I). At first glance the histogram plots suggest a low-temperature chemistry for the $7.25\text{ }\mu\text{m}$ band formation since the abundance varies by less than a factor five towards both low-mass and high-mass sources, including upper limits. Strict upper limits are however not possible to derive because of the inherent weakness of the feature and the low variation is probably due to the high detection threshold rather than to an inherent low variation in abundance of the carrier.

Another possible carrier of the $7.25\text{ }\mu\text{m}$ feature is $\text{CH}_3\text{CH}_2\text{OH}$. A spectral comparison between laboratory data and a *ISO* spectrum of W33A and a *Spitzer* spectrum of B1-b shows that the band widths and band positions of the $7.25\text{ }\mu\text{m}$ features towards the high-mass protostar W33A and the low-mass source B1-b agree better with pure $\text{CH}_3\text{CH}_2\text{OH}$

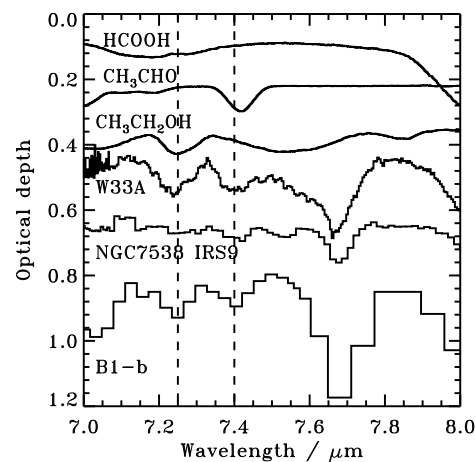


Figure 2.9 – *ISO* spectra at 7–8 μm for W33A, NGC7538 IRS9 and B1-b, following subtraction of a local spline continuum, plotted together with laboratory spectra of pure HCOOH, CH₃CHO and CH₃CH₂OH ices. The dashed lines mark the 7.25 and 7.40 μm features usually assigned to HCOOH and HCOO⁻. The feature at 7.67 μm is due to CH₄ ice.

ice than with pure HCOOH ice (Fig. 2.9). In all protostellar spectra a local spline continuum was fitted to 6.9, 7.16, 7.33, 7.77 and 7.85 μm . Though the HCOOH feature may become somewhat more narrow in ice mixtures (Bisschop et al. 2007a) it still does not fit the observed feature; the mismatch between the width of all plausible HCOOH spectral bands and the width of observed 7.25 μm feature was already noted in Paper I, though the HCOOH identification was still maintained. In a previous study the CH₃CH₂OH abundance was constrained for NGC7538 IRS9 from another CH₃CH₂OH feature at 3.4 μm to be <1.2% with respect to H₂O ice (Boudin et al. 1998). This agrees with the lack of a feature at 7.25 μm . No strong limits can be derived for W33A from the 3.4 μm band or any other bands within the *ISO* spectral range compared with the 7.25 μm feature.

Figure 2.9 also shows that the observed 7.40 μm is more likely due to CH₃CHO rather than HCOO⁻ – both have been proposed previously as carriers (e.g. Schutte et al. 1999; Gibb et al. 2004, Paper I). Hence, while HCOOH and HCOO⁻ cannot be excluded from the ice, their abundances cannot be determined from the 7.25 and the 7.42 μm ice features.

Both CH₃CH₂OH and CH₃CHO are readily formed by UV-induced chemistry in CH₃OH-rich ices (Chapter 10). From the PCA plots, the 7.25 μm band is related to C1 and C2, and possibly to CH₄. C1 and C2 both absorb at the typical position of HCO-bearing species and may thus trace either simple organic molecules such as H₂CO and HCOOH or a complex UV or cosmic-ray-induced chemistry in general, or both. The correlation with CH₄ is curious, but may be explained by an enhanced complex molecule production in the presence of CH₄ (Chapter 10). Though more sources need to be investigated in detail for limits on different complex organics, the combination of C1, C2 and the 7.25

and 7.40 μm features towards protostars may potentially be used as a tracer of a complex ice chemistry. An interesting first step would be to investigate the variability of the 7.25 μm to 7.40 μm ratio and how this relates to the complex ice chemistry investigated experimentally in Chapter 10.

In Paper I, two of the 5-7 μm spectral components, C3 and C4, were tentatively assigned to NH_4^+ , resulting in NH_4^+ abundances of 2–16% with respect to H_2O ice towards the low-mass protostars, 5–26% towards the high-mass protostars and 5–12% towards the background stars. The lack of correlation between NH_3 and C3 and C4 is not inconsistent with the identification of NH_4^+ , since a different fraction of NH_3 may be converted into NH_4^+ in different lines of sight. The NH_4^+ abundances are higher than those of its precursor NH_3 in most lines of sight, suggesting a very efficient conversion from NH_3 to NH_4^+ . This is consistent with acid-base chemistry with strong acids such as HNCO or HCOOH (Schutte & Khanna 2003; van Broekhuizen et al. 2004), which results in almost complete conversions from neutral to ionic form already at 15 K. There are two caveats, however, first the presence of C4 towards background stars is not consistent with its assignment to warm NH_4^+ , and second the production of strong acids must be efficient under quiescent conditions. OCN^- is certainly not the counter ion of NH_4^+ , since the OCN^- ice abundances are an order of magnitude lower than the reported NH_4^+ abundances. If a formation path from hydrogenation of atoms to other strong acids is identified, the NH_4^+ assignment may also be consistent with the lack of variability in C3 with respect to H_2O ice. This is however a big if, and experiments are surely required to test whether such formation paths exist, e.g. the viability of HCOOH formation from partial hydrogenation of CO followed by reaction with OH.

Despite these caveats NH_4^+ remains the most probable main carrier for the C3 band, mainly because of lack of options; the other plausible option is H_2CO , but it was excluded as a major carrier in Paper I because of constraints on other H_2CO features absorbing at 3.34–3.54 and at 5.8 μm , i.e. the position of C1. The C1 and C3 features correlate, albeit weakly ($R=0.42$, 48 detections), when normalized to the water abundances in each line of sight, as might be expected if both features partially share H_2CO as a carrier. A partial assignment of NH_4^+ to C3 therefore seems warranted and possibly to C4, but not the derivation of NH_4^+ abundances from integrating the entire C3 and C4 features.

2.4.2 Early versus late ice formation during low-mass star formation

Figure 2.10 summarizes the conclusions drawn in this section on when and where the identified ices form during the cloud core formation followed by star formation. Unidentified ice features are discussed in relation to the ice formation under ‘early’, ‘late’ and protostellar stages.

Previous ice survey studies noted that some ice abundances, e.g. that of CO_2 , are almost constant towards low-mass sources with respect to H_2O ice, while others, especially the ice abundances of CO, CH_3OH and XCN , vary by more than an order magnitude with respect to H_2O ice (Pontoppidan et al. 2003; van Broekhuizen et al. 2005, Paper II). The

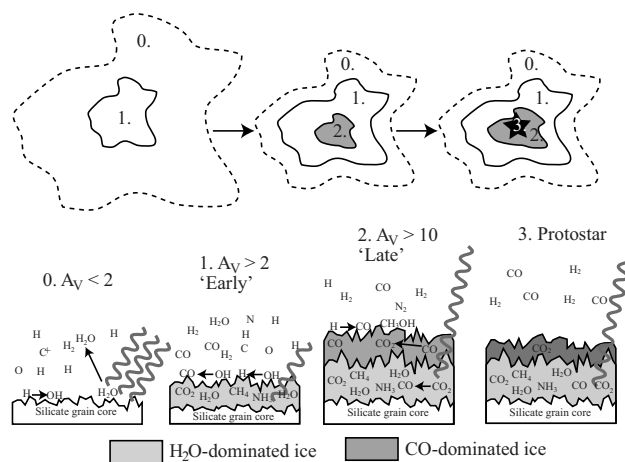


Figure 2.10 – The key ice reactions during the different stages of cloud and star formation. In the protostellar stage desorption of CO starts at 20 K and H₂O:CO₂ segregation at 30 K.

abundance histograms in §2.3.1 visualize these previous conclusions and also show that among the other identified ice features, NH₃ and CH₄ vary little if the large uncertainties in their abundances are taken into account, while all CO and CO₂ ice component abundances, except for CO₂:H₂O, vary by an order of magnitude or more. This difference in ice abundance patterns can be interpreted in terms of early, global cloud formation resulting in narrow distributions versus locally produced ices in the prestellar core or in the protostellar envelope resulting in broad distributions. This interpretation is supported by an early onset of CO₂ ice formation from ice mapping (Bergin et al. 2005) and the fact that ice spectra towards a few background stars contain H₂O and CO₂ ice features, whereas the upper limits of other ‘early’ species such as NH₃ and CH₄ are inconclusive (Knez et al. 2005). Species in Table 2.4 with log-transformed standard deviations <0.2 of the median are thus consistent with early formation in molecular clouds together with H₂O ice.

Figure 2.6 shows that large variations in ice abundances can be explained from different local prestellar conditions and thus large ice variations alone cannot be used as a signpost for ice processing during the protostellar stage. The CO, CO:H₂O, CO₂:CO, CO₂:H₂O and XCN (2175 cm⁻¹ feature) bands all grow with respect to H₂O ice towards the central Oph-F core region. The trends of these abundances towards the core suggests that fast CO accretion towards the core first produces hydrogenated CO (CH₃OH) and species forming from CO and hydrogenated atoms, e.g. CO₂ and HNCO. The latter then loses a proton to NH₃ to form OCN⁻. As H atoms become scarce, reactions between CO and O(H) and energetic processing of both the H₂O and CO-rich ice layers begins to dominate the chemistry towards the cloud core and CO₂:CO, CO:H₂O and OCN⁻ abundances continue to increase. Cosmic rays and secondary UV photons are present throughout the

cloud and thus energetic processing of ices is possible. Some of the 'CO:H₂O' increase may actually be 'CO:H₂CO' and 'CO:CH₃OH' increases instead, which may be the result of UV processing of CH₃OH ice (Chapter 10). The decrease in several ice abundances towards the core can also be understood from quiescent UV and ion processing, which continuously dissociate ices and therefore will result in a lowered ice abundances for species with higher dissociation cross-section than H₂O ice when their production channels are turned off.

The variable C1, C2 and C5 components are not significantly correlated with any of the CO and CO₂ features except for the previously reported tentative correlation between C5 and the CO-component ratios tracing protostellar heating (Paper I). As suggested above, C1, C2 and the 7.25 μ m feature may be associated with complex organic carriers that form in the ice once it has been moderately heated and previously dissociated ices can recombine into larger molecules. The presence of C1 and C2 in clouds shows, however, that they probably have multiple carriers of which some are simple, e.g. H₂CO, and other more complex. The 7.25 μ m feature together with pure CO₂ ice may in the end be the only features that form exclusively in heated ices.

2.4.3 Ice formation in low-mass versus high-mass protostars

The low- and high-mass protostars mainly differ in their CO, CH₄ and CO₂ ice abundances, which are all low towards the high-mass protostars. The low CO and CH₄ abundances can be explained by their high volatility and thus sensitivity to heating. The low CO₂ content can have several possible origins. The time scales for cloud formation and collapse may be different for low- and high-mass stars i.e. faster for the high-mass case, which allows less CO to freeze out and thus less CO₂ to form. Less CO freeze-out and thus less CO₂ formation would also be expected if the cloud spent less time at 20 K. Another possibility is a higher thermal or non-thermal destruction of the CO₂ ice towards the high-mass protostars; the higher irradiation field may photodissociate CO₂ into CO, which subsequently desorbs or CO₂ may simply thermally desorb. A larger high-mass protostellar sample would certainly aid in resolving which process is the dominating one for explaining the low CO₂ content. Such a sample is now just becoming available through new *Spitzer* data (Seale et al. 2009).

There is no evidence for a higher CH₃OH or XCN content towards high-mass stars, except for the single case of W33A. There is thus no evidence for a formation pathway of these species that involves stellar UV irradiation or excess heat. The 7.25 μ m feature seems somewhat more common towards high-mass stars, indicative of a partial UV or thermal ice chemistry origin, consistent with an assignment to CH₃CH₂OH, which forms through diffusion of previously produced ice radicals in the warm envelope (Chapter 10). Of the 5–7 μ m components, C1, C2 and C3 have similar relative optical depths with respect to H₂O ice towards both low-mass and high-mass sources, while the C4 and C5 are shifted to the high-abundance range towards the high-mass stars, again indicative of at least a partial formation pathway involving heat or UV irradiation or both, in agreement with the analysis in Paper I.

Most ice abundances are, however, remarkably similar towards low- and high-mass

protostars, further highlighting the importance of the cold pre-stellar stage for ice formation up to the complexity of CH₃OH.

2.5 Conclusions

Large samples of ice sources are necessary both to identify general trends in the ice evolution and to identify which ice processes always precedes star formation and which depend on the local environment where the protostar forms. The variability of ice abundances, measured by the normalized standard deviation, ranges from 13% to an order of magnitude, stressing the different formation paths of different ices. The low-mass and high-mass protostellar ice abundances only differ significantly for the volatile species CO and CH₄ and for CO₂. There is thus no evidence for a richer UV-induced ice chemistry around high-mass protostars compared to low-mass protostars, as previously supposed.

From ice maps, CO freeze-out together with cosmic ray induced processing (through either direct ion bombardment or secondary UV photons) and atomic processing can produce local differences in ice abundances within the same cloud. In contrast, a principal component analysis (PCA) on the low-mass sample reveals that there is no overall, significant difference in ices between the investigated clouds. The PCA reveals a number of new correlations between the tentatively identified or unidentified features in the spectra with known ice species, e.g. between the 7.25 μm band and features at 5.8 and 6.2 μm , all which potentially trace more complex ices. The PCA also suggest that most of the variation in the data set is connected with the total CO₂ and CO ice content, the CO versus CO₂ content or ice temperature and the production of more complex species. This is consistent with the analysis of the single core Oph-F and of the abundance variations. PCA is thus a useful tool to get an overview of a large set of data – here more than 50 sources and 19 unique ice components.

A re-evaluation of previous assignments of the 5–7 μm components, and the 7.25 and 7.40 μm features has put the common assignments of the 7.25 and 7.40 μm features to HCOOH and HCOO⁻ into question – CH₃CH₂OH and CH₃CHO agree better with the observed band positions and band widths alike. The large amounts of NH₄⁺ tentatively reported previously should also be taken as upper limits, until more laboratory data becomes available. In general the field is in dire need of both sensitive, high-resolution spectral observations of ices in protostellar envelopes and towards background stars as well as quantitative laboratory work on the proposed formation paths of most ices.

The combined results from the ice abundance histograms, ice maps, correlation plots and PCA suggest an ice formation scenario through the following steps:

1. H₂O, CO₂, CH₄, NH₃ form through hydrogenation and oxygenation of atoms and small molecules at low cloud densities, when the gas phase is still rich in atoms. Some of the NH₃ is converted to NH₄⁺ through acid-base chemistry in the presence of quiescently produced acids.
2. Deeper into the cloud or at later times during the cloud collapse, CO freezes out catastrophically on top of the previous H₂O-rich ice. Some of the CO is converted

into H_2CO and CH_3OH , dependent on the H/H_2 ratio in the gas phase, and CO continues to react with OH to form CO_2 and probably with NH to form HNCO . HNCO reacts to form OCN^- in the presence of NH_3

3. All through the cloud evolution, the CO - and H_2O -rich ices are further processed by cosmic rays and cosmic-ray induced UV radiation (Shen et al. 2004). This together with CO reactions with heavier atoms become the dominant driver for ice evolution after the gas phase has been depleted of H and H processing is no longer possible. The result is $\text{CO}_2:\text{CO}$, $\text{CO}:\text{H}_2\text{O}$ ice mixtures and the continued production of OCN^- .
4. Once the protostar turns on, ices start to become mobile, resulting in radical diffusion, ice desorption and segregation. The proposed complex carriers of the C1 and C2 components and the $7.25 \mu\text{m}$ band may be associated with this ice formation phase. More background sources are however needed to check that complex ices cannot form prior to the onset of star formation and also a dedicated analysis towards which protostars the $7.25 \mu\text{m}$ band appears. Ice heating definitely results in pure CO_2 ice formation through ice distillation and segregation, and in CO and CH_4 evaporation. The C4 and C5 components and the XCN band assigned to OCN^- are all tentatively dependent on ice temperature.